Automated 3-D Piping Routing Synthesis Considering Seismic Resilience: Part II—Algorithmic Characterization, Statistical Assessment, and Proof-of-Concept Validation*

Shunta Mogi
Waseda University
3-4-1 Okubo, Shinjuku, Tokyo 1698555, Japan

Naoya Takamura
Department of Mechanical Engineering, Yamaguchi University
2-16-1 Tokiwadai, Ube, Yamaguchi 7558611, Japan

Akane Uemichi, Ph.D.†
Department of Mechanical Engineering, Yamaguchi University
2-16-1 Tokiwadai, Ube, Yamaguchi 7558611, Japan
E-mail: uemichi@yamaguchi-u.ac.jp
ASME Member

ABSTRACT

Stochastic optimization algorithms, such as the Multi-Objective Genetic Algorithm (MOGA) integrated into the MOGA-A* framework established in Part I, enable automated 3-D

---

* This is a pre-peer-reviewed version of the manuscript.

† Corresponding author.

Email: uemichi@yamaguchi-u.ac.jp

pathfinding in plant engineering. However, their inherent stochasticity introduces trial-to-trial geometric variability, raising reliability concerns for safety-critical applications. To evaluate the operational capabilities and limitations of this lightweight surrogate-driven solver, this paper (Part II) presents a three-part empirical assessment. First, to quantify search-space reproducibility, a computational sweep of 1,000,000 candidate layouts across distinct spatial topologies was conducted. Maximum Likelihood Estimation confirmed that compliant total evaluation indices follow predictable log-normal or gamma distributions, parameterized by a topological Designable Space Ratio metric incorporating space occupancy and obstacle clustering. Second, to assess whether the response-spectrum modal surrogate captures relative physical dynamic trends rather than absolute stress magnitudes, frequency-sweep shaking-table experiments were performed on 1:50 scaled models. The experiments reproduced the predicted downward shift in the dominant modal frequency and confirmed a lower peak dynamic response for the synthesized flexible-detour layout, which exhibited a 45.7% reduction in the experimentally derived response metric (11.98 MPa) relative to the unoptimized baseline (22.08 MPa). Third, to assess real-world decision-support utility, an algorithmically synthesized layout was benchmarked against a baseline manually drafted by an experienced engineer under identical spatial constraints from the Onagawa Nuclear Power Plant. Although the human designer achieved a lower peak dynamic stress (18.63 MPa vs. 145.46 MPa) by incorporating higher intermediate support density, the automated solver generated a code-compliant, collision-free candidate in 46 minutes. These results demonstrate that while support allocation heuristics benefit from post-processing refinement, the MOGA-A* framework functions as an effective decision-support engine that automates initial spatial pathfinding and reduces manual trial and error in early-stage plant design.

1. INTRODUCTION

The integration of automated routing methodologies into the detailed design of pressure vessels and piping systems represents a critical shift toward digital transformation in plant engineering [1]-[3]. Over the past decades, various deterministic pathfinding techniques, such as Lee's algorithm [4] and Dijkstra's search, as well as stochastic metaheuristics [5], have been explored for 3D spatial layout generation. Recently, hybrid approaches that combine deterministic local pathfinders (e.g., A*) with multi-objective evolutionary algorithms (MOGA) have demonstrated high potential for solving complex multi-constraint routing problems in shipbuilding and process plants [6]-[8]. As formulated and computationally verified in Part I of this investigation, our proposed MOGA-A* framework successfully addresses the dual challenges of 3-D spatial collision avoidance and dynamic seismic stress mitigation [9]. By utilizing response spectrum modal analysis—a standard lightweight structural evaluation method in nuclear piping standards such as JEAC 4601 [10] and ASME BPVC Section III [11]—as a structural surrogate model, the Part I framework autonomously synthesizes flexible detour topologies (e.g., expansion loops) that decouple the piping system from destructive seismic floor-resonance peaks [12].

However, from a scholastic and industrial design perspective, the deployment of such stochastic evolutionary metaheuristics in safety-critical industries (e.g., nuclear power generation and chemical refineries) is constrained by strict requirements for algorithmic reliability, statistical reproducibility, and physical verifiability [15], [16]. Because the Part I framework relies on a stochastic mid-waypoint generation strategy to bypass local minima [9], the final converged routing configurations inevitably exhibit trial-to-trial geometric variations under identical spatial boundary conditions [17]. In the context of decision-support systems, this stochastic variability poses a fundamental engineering challenge: a structural design tool cannot be treated as a mere "black-box" heuristic; its search-space characteristics must be quantitatively characterized [17],[18].

Furthermore, the framework's reliance on a lightweight spectral modal analysis as a surrogate for full non-linear FEM necessitates empirical evaluation to verify whether relative structural rankings translate consistently to physical dynamic trend [19],[21]. The robustness and initial-value dependence of Genetic Algorithms have been extensively debated within the computational intelligence community [15],[18]. While stochastic metaheuristics are proficient at escaping local optima, their inherent reliance on pseudo-random operations introduces trial-to-trial variability that can compromise the search space's ergodicity in highly constrained, non-convex topologies [17]. To mitigate this variability, numerous robust optimization frameworks and surrogate-assisted evolutionary computation schemes have been proposed to evaluate how algorithmic parameters, population diversity, and constraint-handling mechanisms influence the reliability of convergence under uncertainty [16]. Furthermore, characterizing fitness landscape topography through large-scale computational sampling is now recognized as an essential protocol for deploying these optimization tools in safety-critical engineering applications [17], [18]

Building upon the optimization framework established in Part I [9] and preliminary findings in Ref. [14], this paper (Part II) evaluates the operational capabilities and limitations of the MOGA-A* solver through systematic statistical and empirical assessments. Specifically, this investigation addresses three key engineering questions:

1. **Statistical Characterization of Stochastic Variability:** How does spatial clutter influence trial-to-trial variability and local-minima trapping, and how many parallel optimization runs are estimated to retrieve a high-performance routing candidate?
2. **Proof-of-Concept Physical Assessment of Dynamic Trends:** Do relative structural rankings and modal shift trends captured by the lightweight spectral surrogate reflect physical dynamic behavior observed in scale-model shaking-table tests?
3. **Engineering Utility Assessment Against Human Expertise:** How does the algorithmically synthesized layout compare with a manual baseline created by an experienced designer under identical spatial and structural constraints?

First, Section 5 characterizes search-space topography across four spatial configurations through a computational sweep of 1,000,000 candidate evaluations. By introducing a topological metric that incorporates volumetric space occupancy and obstacle clustering, Maximum Likelihood Estimation probability models are established to quantify search reproducibility.

Next, Section 6 evaluates physical dynamic trends through a proof-of-concept shaking-table assessment on a 1:50 scaled model. Subjecting an unoptimized rigid baseline and a synthesized flexible layout to dynamic frequency-sweep excitations, non-contact laser displacement measurements verify whether surrogate-based structural rankings correspond to observed physical response reductions.

Finally, Section 7 assesses real-world engineering utility by benchmarking an algorithmically synthesized layout against a manual baseline drafted by an experienced nuclear piping designer using actual Onagawa Nuclear Power Plant blueprints. This comparison delineates practical trade-offs between manual expert routing and physics-informed algorithmic synthesis, highlighting benefits such as automated execution, multi-candidate Pareto generation, and parallel design workflows.

Through this multi-tiered assessment, Part II establishes the statistical reproducibility, physical dynamic consistency, and decision-support utility required to deploy lightweight surrogate-driven evolutionary synthesis in early-stage plant facility engineering.

2. THE DESIGNABLE SPACE RATIO AND STRUCTURAL COMPLEXITY

In this study, the "designable space ratio" was defined as an index of the designable space for piping design within the design space. First, the designable space ratio is defined. The designable space ratio is an index that indicates how much room is available for piping routing due to the installation of equipment or other structures in the piping routing space.

The purpose of setting the designable space ratio in this study is to use it as a numerical index to determine whether the design space needs to be optimized. For example, if the design space is mostly filled with obstacles, the available space for pipe routing is very limited. In this case, no optimization can be performed, or the piping layout can be determined without optimization. In other words, there is no need for optimization.

Lee et al. [20] have focused on the designable space of piping. For problems with a small designable space, the time can be further reduced by reducing the number of calculations. The calculation amount can be reduced when the designable space is small, as in Ref. [20]. Conversely, when the designable space is large, the number of piping layouts to be evaluated increases because many layouts can be designed. As a result, the computational complexity increases. However, considering many piping layouts can be an advantage, especially for seismic resistance. This is because the seismic resistance of pipes of the same length varies with the layout and support locations.

Before analyzing the detailed routing results, it is essential to establish a mathematical framework for evaluating the structural complexity of routing environments. We proposed the designable space ratio g_{DSR} as a dimensionless index that quantifies the available spatial clearance for piping routing. This parameter indicates that the volumetric constraints and spatial layout of solid obstacles significantly compress or expand the viable path options, directly impacting computational efficiency and search reproducibility. The parameter g_{DSR} is defined using the normalized space occupancy index $\hat{g}_{Occ}$ and obstacle index $g_{cluster}$ as below:

$$g_{DSR} = \hat{g}_{Occ} g_{cluster} \tag{1}$$

The space occupancy index, g_{Occ}, represents the volume of the design space occupied by solid obstacles, modeled via a log-normal distribution:

$$g_{Occ}(\mu_V, \sigma_V) = \frac{1}{(1-\mu_V)\sigma_V\sqrt{2\pi}} \exp\left\{-\frac{(\ln \mu_V - 0.5)^2}{2\sigma_V^2}\right\} \tag{2}$$

where μ_V is the volume ratio of obstacles to the total design space, defined as $\mu_V = V_{obs}/V$; here, V_{obs} is the aggregate volume of solid obstacles [m^3], and V is the global design volume [m^3]. The shape parameter that controls the distribution's sensitivity is denoted as σ_V. In this study, $\sigma_V = 1.09$ is selected as a fitting constant to satisfy the physical boundary conditions: it retains a baseline evaluation margin when the space is empty ($\mu_V = 0$) and smoothly converges to zero as the space becomes fully congested ($\mu_V \to 1.0$).

Based on this formulation, the spatial routing complexity theoretically peaks when μ_V reaches 0.5. This is because a half-occupied space geometrically generates the maximum number of narrow topological corridors and routing diversities, unlike completely empty or fully blocked environments. Therefore, the index is normalized to its maximum value at this peak as $\hat{g}_{Occ} = g_{Occ}(r_V)/g_{Occ}(0.5)$. The resulting log-normal distribution of the space-occupancy index $\hat{g}_{Occ}$ is shown in Figure 1.

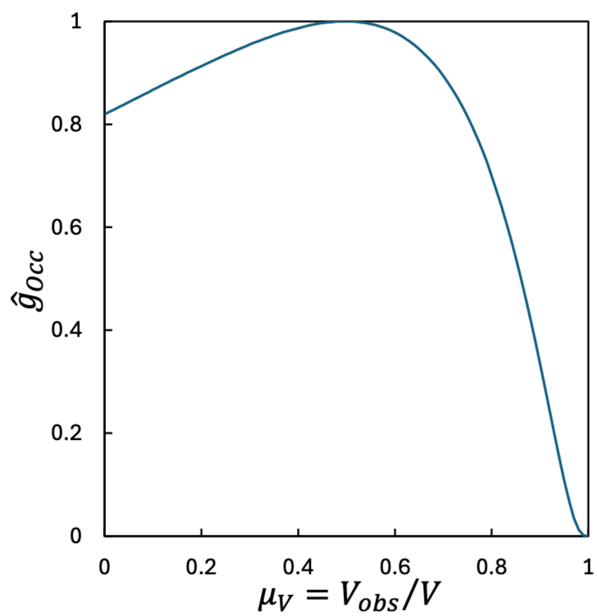

Figure 1: Distribution of the normalized space occupancy index $\hat{g}_{Occ}$ against the total volume ratio of obstacles, modeled as a log-normal distribution peaking at $\mu_V = 0.5$.

The obstacle clustering index, $g_{cluster}$, penalizes the spatial dispersion of these solid volumes using hierarchical agglomerative clustering:

$$g_{cluster} = \frac{1}{1.05^{n_{\text{cluster}}}} \quad (3)$$

where $n_{cluster}$ is the number of distinct obstacle groups determined by evaluating the Euclidean distance threshold. Based on the integration of these two constituent indices, the overall 3-D topological distribution of g_{DSR} is shown in Figure 2. The g_{DSR} reaches its theoretical maximum of 1.0 in a completely unobstructed space and asymptotically approaches 0 as the number of distinct obstacle clusters and volumetric occupancy increase.

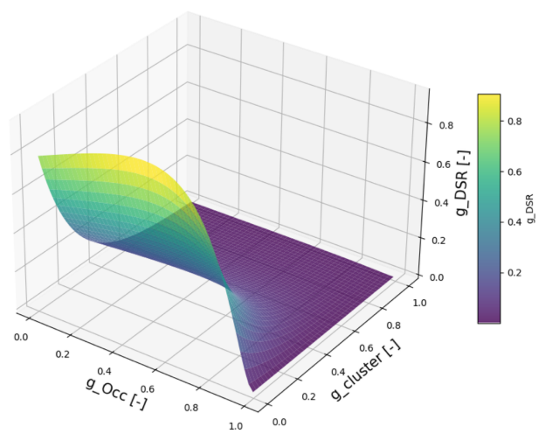

Figure 2: 3-D distribution of the Designable Space Ratio g_{DSR} plotted against the space occupancy ratio g_{Occ} and the number of obstacle clusters g_{cluster}.

3. Simulation Case Settings and Obstacle Coordinates

3.1. Common Design Space and Equipment Terminal Settings

The global 3-D search space is modeled as a continuous Cartesian bounding volume. Starting and ending nozzle coordinates are identical across all simulation cases.

- Design Space Volume (L_x, L_y, L_z): 32.0 m by 60.0 m by 20.0 m

- Start Point Terminal (x_s, y_s, z_s): (7.0, 0.0, 17.0) m
- End Point Terminal (x_e, y_e, z_e): (30.0, 60.0, 2.0) m

3.2. Obstacle Configurations and Layout Figures for Cases 1, 2, 3, and 4

To evaluate search-space ergodicity and topological characteristics as structural complexity increases, four obstacle configurations were established. The coordinates, dimensions, and layout figures for each case are presented below. Figure 3 and

Table 1 present each case.

Case 1: Onagawa-Derived Benchmark Layout

Case 1 replicates the spatial clutter found in actual nuclear facility blueprints, featuring five asymmetric rectangular obstacle groups at varying heights to create overlapping keep-out zones.

Case 2: Dual-Obstacle Layout

Case 2 evaluates topological bifurcation. Two large, continuous barriers bisect the central design volume, forcing a choice between left and right detour corridors.

Case 3: Highly Fragmented Layout

Case 3 tests global exploration in highly fragmented spaces. Five small, symmetrical obstacles are dispersed throughout the volume to create narrow, disjointed corridors.

Case 4: Congested Model Layout

In Case 4, obstacles were placed within a design space with the same start and end points as Problems 2 and 3, such that the designable space ratio is 0.50.

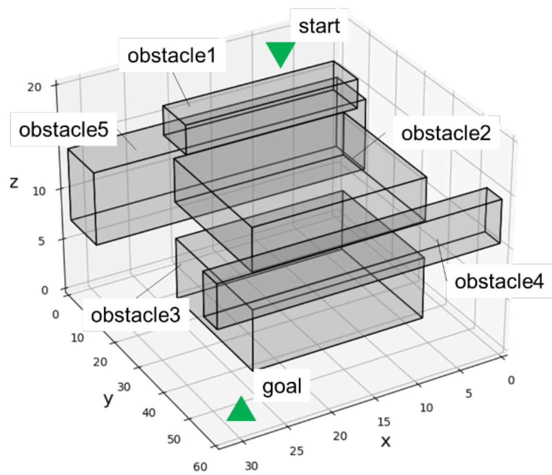

(a) Case 1 (Onagawa Nuclear Power Plant model, g_{DSR} = 0.88)

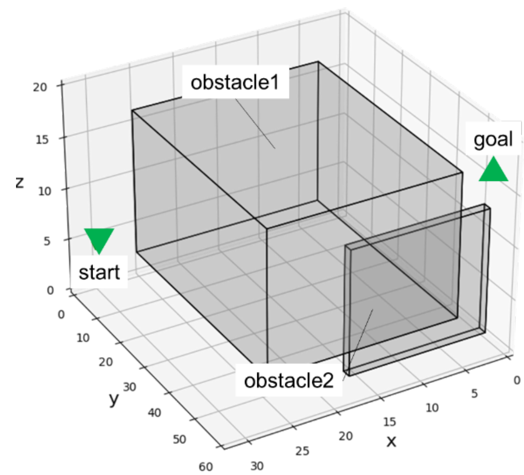

(b) Case 2 (Dual-obstacle model, g_{DSR} = 0.95)

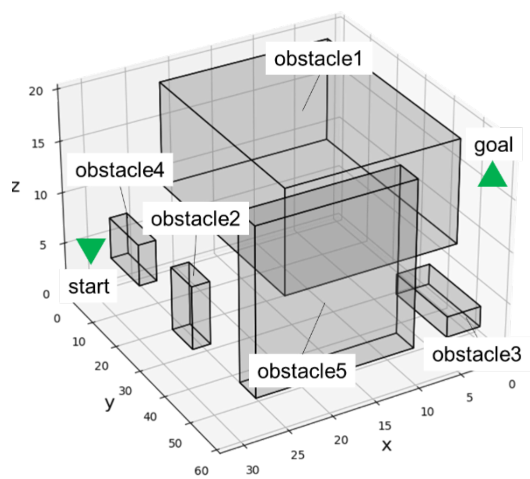

(c) Case 3 (Five-block model, g_{DSR} = 0.89)

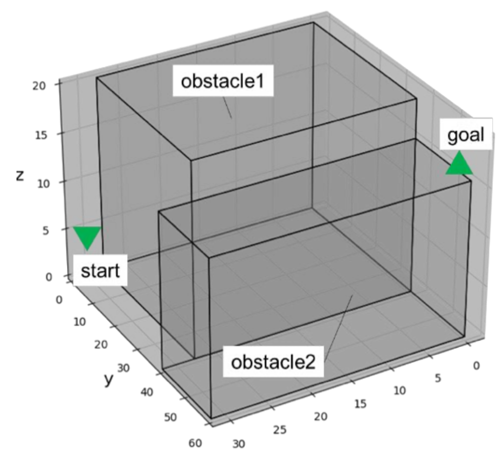

(d) Case 4 (Two-block model, g_{DSR} = 0.50)

Figure 3: 3D spatial layout of obstacles and synthesized routing corridors.

Table 1: Obstacle Coordinates and Bounding Dimensions

(a) Case 1

	x	y	z	w_x	w_y	w_z
Obstacle1	14	15.5	17.2	20	9	2.8
Obstacle2	14	30.0	12.3	20	30	4.2
Obstacle3	14	30.0	3.6	20	30	6.0
Obstacle4	16	56.5	12.3	30	5	4.2
Obstacle5	16	5.5	10.5	32	11	7.0

(b) Case 2

	x	y	z	w_x	w_y	w_z
Obstacle1	15	29	10	22	52	14
Obstacle2	10	58	8	16	2	12

(c) Case 3

	x	y	z	w_x	w_y	w_z
Obstacle1	12	26	14	20	48	10
Obstacle2	29	38	7	2	8	6
Obstacle3	3	47	3	4	18	2
Obstacle4	28	11	6	2	12	4
Obstacle5	19	56	11	18	6	16

(d) Case 4

	x	y	z	w_x	w_y	w_z
Obstacle1	14	20	10	14	20	10
Obstacle2	16	50	8	16	10	8

By introducing this mathematical indicator, we can quantitatively define and compare the routing complexity of the simulation environments. Specifically, the framework was tested across four primary spatial configurations that represent increasing complexity: Case 1 (g_{DSR} = 0.88), Case 2 (g_{DSR} = 0.95), Case 3 (g_{DSR} = 0.89), and Case 4 (g_{DSR} = 0.50).

3.3. Genetic Algorithm Control Parameters

This section defines the default control parameters for the Multi-Objective Genetic

Algorithm (MOGA) used in automated routing optimization across all evaluated simulation cases as shown in Table 2.

Table 2: Parameter Settings of the Genetic Algorithm

Number of generations	100
Population size	100
Crossover ratio	0.85
Mutation ratio	5%

4. CASE STUDIES AND MULTI-ANGLE EVALUATION OF ROUTING CANDIDATES

To evaluate the capabilities of the proposed hybrid Multi-Objective Genetic Algorithm and deterministic A* (MOGA-A*) framework across varying structural and spatial conditions, numerical routing optimizations were conducted for Cases 1, 2, and 3, representing designable space ratios g_{DSR} of 0.88, 0.95, and 0.89, respectively. In addition to monitoring the baseline evolutionary convergence over 100 generations, alternative Pareto-optimal candidates targeting individual objectives were evaluated to provide actionable design drafts for practical plant engineering.

4.1. Algorithmic Convergence and Spatial Routing Performance

Across all evaluated spatial configurations, the hybrid framework successfully demonstrated spatial collision avoidance ($P_O = 0$) while simultaneously minimizing piping length, bend counts, and redundant supports. The quantitative optimization performance and objective breakdowns across 100 generations for Cases 1–3 are summarized in Table 3.

Table 3: Optimization performance and objective breakdown across Case Studies

Case Study	Spatial Complexity (g_{DSR})	Generation	Total Evaluation (F)	Peak Stress [MPa]	Pipe Length [m]	Bend Count	Interference
Case 1	0.88	Initial (1st)	11.82	48.52	98.0	7	Yes
		Final (100th)	0.80	145.46	98.0	4	No
Case 2	0.95	Initial (1st)	2.19	120.	106.0	6	No
		Final (100th)	0.62	89.13	102.0	3	No
Case 3	0.89	Initial (1st)	2.53	> 350.0**	108.0	6	No
		Final (100th)	0.54	64.76	102.0	3	No

** Stress values exceeding 350.0 MPa indicate that the unoptimized initial routing layout violated structural response spectrum limits prior to evolutionary convergence.

In Case 1, representing the Onagawa Nuclear Power Plant model, the elite solution evolved from an initial seven-bends layout to a simplified four-bends detour, causing the overarching evaluation index F to decrease from 11.82 to 0.80. In Case 2, F decreased from 2.19 to 0.62, driven primarily by bend-count reduction because the presence of large central clearance spaces maintained peak dynamic stress at relatively low values throughout the search. Case 3 exhibited non-convex fitness landscape characteristics, where F remained plateaued near 1.24 until the 76th generation. At the 77th generation, a targeted mutation operator eliminated an unnecessary vertical waypoint, enabling the local A* pathfinder to instantly construct a direct horizontal corridor and yielding a sharp step-change improvement in both dynamic and overall length.

4.2. Physics-Informed Trade-Offs and Alternative Pareto Candidates

Analysis of the multi-objective search trajectory reveals fundamental physical interactions between routing topology and structural dynamic resilience. Minimizing geometric length alone tends to increase system stiffness, inadvertently shifting fundamental natural frequencies into floor-resonance peaks. Conversely, introducing flexible S-curve detours decreases overall stiffness, successfully decoupling the structure from seismic excitation peaks and drastically lowering dynamic bending stresses. Evaluating single-objective Pareto alternatives alongside balanced elites further demonstrates the practical flexibility of the synthesized layouts. For Case 1, a candidate prioritizing seismic performance achieved a peak dynamic stress of 20.21 MPa, representing an 86.1% reduction compared to the balanced elite's 145.46 MPa. On the other hand, a candidate minimizing bend count achieved the theoretical minimum of two bends; however, the resulting straight segments exceeded the allowable support span threshold of 9.23 m, inducing unacceptable dynamic stresses and confirming the necessity of multi-objective balancing. Similar trade-offs were observed in Cases 2 and 3: a Case 2 alternative at the 95th generation yielded a 63.4% stress reduction (down to 32.63 MPa) over the final elite, while a Case 3 alternative achieved a 27.3% stress reduction (down to 47.09 MPa), both remaining comfortably below the regulatory allowable limit of 309 MPa [10]. These comparisons verify that while the primary elite provides a practical starting point, assessing alternative candidates equips plant engineers with structurally robust options tailored to specific operational priorities.

5. REPRODUCIBILITY, STATISTICAL ROBUSTNESS, AND SENSITIVITY ANALYSES

5.1. Background and Problem Statement for Statistical Evaluation

The hybrid MOGA-A* optimization framework provides superior search capabilities in high-dimensional spatial domains subject to structural dynamics. However, because stochastic evolutionary metaheuristics rely on pseudo-random operations during initial population generation and genetic operations (crossover and mutation), trial-to-trial variability in converged routing topologies and evaluation indices is inherently unavoidable.

In safety-critical industrial applications, such as nuclear power generation facilities and chemical refineries, optimization tools cannot be treated as mere "black-box" heuristics. For such decision-support systems to be deployed effectively in real-world engineering workflows, the probability of reaching high-performance candidates, as well as the rate of local-minima trapping and initial-value dependence, must be rigorously quantified from mathematical and statistical perspectives. Accordingly, this section conducts a large-scale computational sampling sweep to characterize the topography of the fitness landscape and evaluate the statistical reproducibility and practical reliability of the proposed framework.

5.2. Large-Scale Statistical Distributions and Probability Density Characteristics

To evaluate search-space ergodicity and reproducibility, 100 independent, parallel optimization trials were conducted with distinct pseudo-random seeds across Case 1, Case 2, and Case 3, each representing different spatial complexities. Each trial evaluated 10,000 individuals over 100 generations, building a large-scale statistical database containing 1,000,000 unique candidate piping layouts per case.

From this candidate pool, structurally compliant populations that satisfy both spatial collision avoidance (P_O = 0) and regulatory response spectrum modal stress ceilings ($S_{\max}$ < 309 MPa) were isolated. Maximum Likelihood Estimation (MLE) was subsequently performed to fit probability density functions to both the overarching evaluation index F across all compliant candidates and the final 100th-generation elite solutions across the 100 independent runs. The quantitative statistical parameters and MLE fitting results are summarized in Table 4. Conceptual probability density distributions and generational elite histograms illustrating unimodal and bimodal convergence patterns are shown in Figure 4.

Table 4: Statistical reproducibility metrics and MLE fitting parameters across benchmark cases

Analysis Case	**Spatial Complexity Index (g_{DSR})**	**Compliant Candidates (out of 10^6)**	**Absolute Minimum Index $F_{\min}$**	**Compliant Population MLE Fit (R^2)**	**High-Performance Band (F Range)**	**Single-Run High-Performance Success Rate (P)**	**Required Parallel Runs N (95%+ cumulative success probability)**
Case 1	0.88 (Onagawa Benchmark)	728,500	0.67	Log-normal (R^2 = 0.941)	[0.75, 0.83]	54.0%	4 (P_{95} = 97.9%)
Case 2	0.95 (Dual Obstacle Model)	754,000	0.54	Gamma (R^2 = 0.937)	[0.54, 0.60]	39.0%	6 (P_{95} = 96.3%)
Case 3	0.89 (Fragmented Obstacles)	713,300	0.54	Gamma (R^2 = 0.941)	[0.54, 0.70]	14.0%	20 (P_{95} = 95.1%)
Case 4	0.50 (Congested Model)	723,600	0.54	Log-normal (R^2 = 0.923)	[0.54, 0.68]	41.0%	6 (P_{95} = 97.1%)

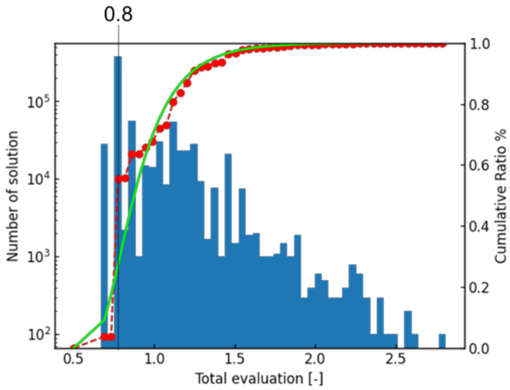

(a) Case 1

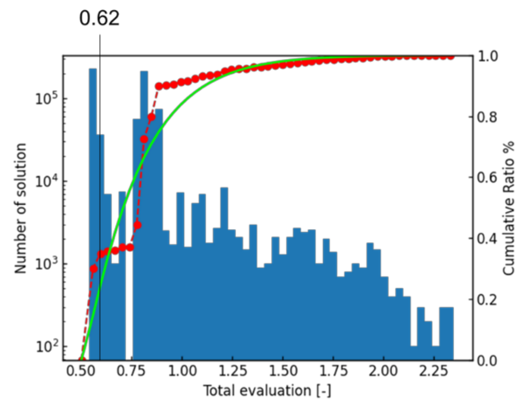

(b) Case 2

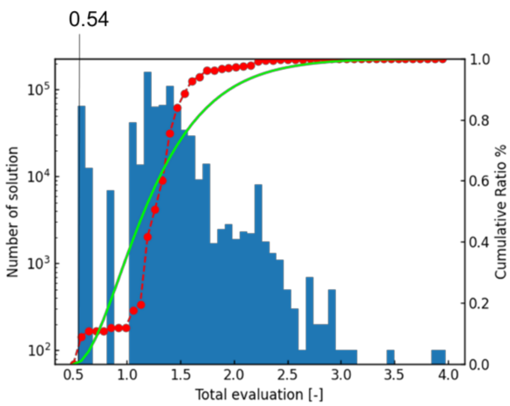

(c) Case 3

Figure 4: Probability density distributions of evaluation index F and 100th-generation elite solutions showing unimodal and bimodal convergence patterns.

In Case 1 (g_{DSR} = 0.88), which models an actual nuclear facility layout, 728,500 candidate evaluations met all structural requirements. MLE analysis was used to fit probability density functions to the overarching compliant fitness distribution, with information criteria and goodness-of-fit testing favoring a log-normal profile (AIC = 1240.2, R^2 = 0.941, K-S test p = 0.12). Evaluating the final 100th-generation elite solutions across 100 independent trials revealed an empirical single-run success probability of 0.540 (95% CI: 44.2%-63.6%) for convergence within the predefined high-performance band of F = [0.75, 0.83]. Applying the cumulative success formulation ($P_N = 1-(1-p)^N \geq$ 0.95) shows that N = 4 to 5 parallel runs yields an estimated probability of 95.5% to 97.9% of retrieving a high-performance candidate layout that satisfies the adopted allowable stress ceiling, demonstrating predictable algorithmic performance.

In Case 2 (g_{DSR} = 0.95), where two large central obstacles bisect the interior design volume, MLE and model selection criteria favored a Gamma distribution profile for the overarching compliant population (AIC = 1185.6, R^2 = 0.937, K-S test p = 0.09). However, the 100th-generation elite solutions exhibited a distinct bimodal distribution. This bimodal behavior is driven by a topological bifurcation occurring in early generations, in which the population stochastically commits to either the left or right macro-corridor. Once converged into a specific corridor basin of attraction, local evolutionary optimization operates within that macro-path, causing the elite population to split between the predefined high-performance band ($F = [0.54{,}0.60]$, 39 runs, corresponding to an empirical single-run success probability of $p = 0.390$, 95% CI: 29.9%–48.9%) and a localized plateau ($F = [0.81{,}0.87]$, 53 runs). Executing $N = 6$ parallel runs yields an estimated cumulative probability of $P_N = 96.3\%$ of retrieving a candidate layout within the high-performance band.

In Case 3 ($g_{\mathrm{DSR}} = 0.89$), featuring five smaller obstacles dispersed throughout the design space, Maximum Likelihood Estimation and model selection criteria favored a Gamma distribution profile for the overarching compliant population (AIC $= 1412.1, R^2 = 0.941$, K-S test $p = 0.07$). However, the 100^{th}-generation elite solutions exhibited lower single-run convergence efficiency, yielding an empirical success probability of $p = 0.140$ (95% CI: 8.2%–22.6%) for reaching the predefined high-performance band ($F = [0.54{,}0.70]$, 14 runs). Most independent runs (68%) remained trapped in localized plateaus ($F = [1.00,1.50]$). Applying the cumulative success formulation ($P_N = 1 - (1-p)^N \geq 0.95$) indicates that executing approximately $N = 20$ parallel runs yields an estimated probability of $P_{20} = 95.1\%$ of retrieving a layout within the high-performance band. This behavior demonstrates that fragmented obstacle networks slice the search volume into narrow, disjointed corridors, creating numerous local minima traps where fitness values remain plateaued until stochastic operators trigger a topological breakthrough. Algorithmic Sensitivity and the Impact of Spatial Obstacle Clustering

To evaluate strategies for mitigating local-minima trapping and improving convergence toward high-performance candidate regimes, sensitivity analyses were conducted by manipulating genetic hyper-parameters and spatial boundary geometries.

First, to evaluate the effect of mutation probability in Case 2 (where topological bifurcation split the population), the baseline mutation rate of 5% was doubled to 10% across 100 independent parallel trials, yielding 723,600 compliant candidate evaluations. The overall distribution of total evaluation index F and the cumulative ratio curve for Case 2 under a 10% mutation rate are illustrated in Figure 5. Statistical analysis revealed that while doubling the mutation probability did not significantly alter the frequency of reaching the predefined high-performance band (F = [0.54, 0.60], 38 runs vs. 39 runs in the baseline), it substantially improved the distribution of suboptimal runs. Specifically, the number of runs trapped in the higher-evaluation plateau (F = [0.81, 0.86]) dropped sharply from 53 to 25, while the intermediate regime (F = [0.76, 0.81]) expanded from 12 to 34 runs. This statistical shift demonstrates that while elevated mutation rates do not necessarily increase the frequency of convergence toward the high-performance band, they effectively help trapped populations escape suboptimal local plateaus and migrate toward lower-evaluation regions of the search landscape.

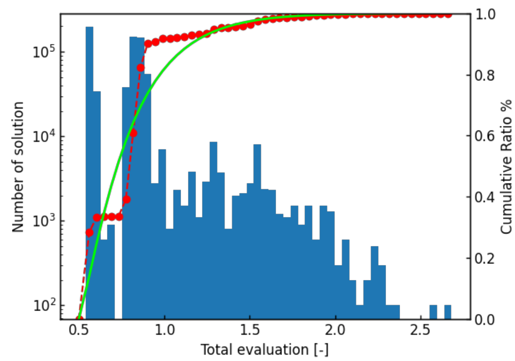

Figure 5: Histogram and cumulative ratio of total evaluation index F for Case 2 under an elevated mutation probability of 10%.

Second, to isolate the effect of spatial constraints on search efficiency, Case 4 was evaluated in a congested environment (g_{DSR} = 0.50) featuring two large obstacle blocks. As shown in Figure 6, despite high volumetric space occupancy (g_{Occ}), 41.0% of independent runs successfully converged to the predefined high-performance band (F = [0.54, 0.68], corresponding to an empirical single-run success probability of p = 0.410, 95% CI: 31.7%-50.9%).

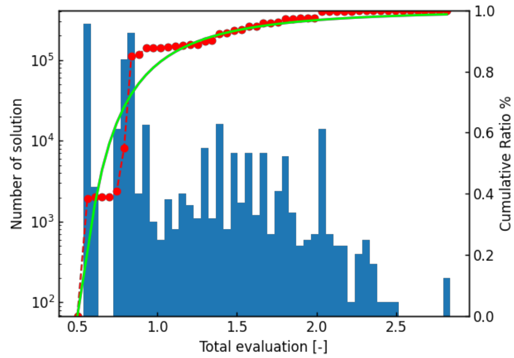

Figure 6: Histogram and cumulative ratio of total evaluation for Case 4

Comparing Case 4 (p = 0.410) with Case 2 (g_{DSR} = 0.95, p = 0.390) and Case 3 (g_{DSR} = 0.89, p = 14.0) indicates that algorithmic search performance in the cases examined appears to be more strongly associated with the obstacle clustering index ($g_{cluster}$) alone. In Case 3, dispersed obstacles fragment the design volume into narrow, disjointed corridors, increasing local-minima trapping. Conversely, in Case 4, large obstacle blocks preserve continuous macro-corridors despite high spatial occupancy, enabling the algorithm to efficiently navigate toward high-performance candidate paths.

5.3. Conclusions on Reproducibility and Industrial Utility

The multi-case statistical evaluations demonstrate that the hybrid MOGA-A* piping routing framework provides predictable search performance across distinct spatial topologies. Depending on the spatial complexity regime, executing N = 4 to 6 independent parallel trials for moderately congested spaces (Cases 1, 2, and 4) or approximately N = 20 trials for highly fragmented spaces (Case 3) yields an estimated cumulative probability exceeding 95% ($P_N \geq$ 95 %) of retrieving at least one candidate layout within the predefined high-performance band that satisfies the adopted allowable seismic stress ceiling.

By demonstrating that stochastic trial-to-trial variability can be empirically characterized and bounded, this investigation indicates that the proposed framework supports its use as an automated decision-support engine for early-stage industrial plant design.

6. PHYSICAL ASSESSMENT VIA DYNAMIC SHAKING-TABLE EXPERIMENTS

6.1. 2D Design Space Formulation, Algorithmic Routing, and Numerical Convergence

While the response spectrum surrogate model in the MOGA-A* framework enables computationally efficient spatial evaluation in 3-D, evaluating whether its relative structural rankings correspond to physical dynamic trends is an important step for decision-support tools in plant engineering. To obtain clear empirical measurements without introducing complex 3-D optical-tracking errors, a 2-D planar routing domain was evaluated as a proof of concept. Planar modeling isolates in-plane vertical bending modes from out-of-plane torsional effects, allowing non-contact laser displacement sensors to measure dynamic vertical bending displacements with high spatial precision. Accordingly, the objective of the experiment is not to validate the absolute stress magnitudes predicted by the response-spectrum surrogate, but to assess whether the surrogate captures modal-frequency shifts and relative dynamic-response rankings between alternative routing geometries.

The 2-D design domain was defined with a full-scale prototype dimension of L_y = 75.0 m in length and L_z = 25.0 m in height. Equipment terminal nozzles were placed at starting coordinates (y_s, z_s) = (0.0, 1.0) m and ending coordinates (y_e, z_e) = (75.0, 23.0)

m. To simulate spatial congestion, 10 rectangular obstacle blocks were distributed across the design space, as defined in Figure 7(a) and Table 5.

Table 5: Bounding dimensions and spatial coordinates of obstacles in the 2D assessment benchmark

	Center $\boldsymbol{y}$ (m)	Center $\boldsymbol{z}$ (m)	Width $\boldsymbol{w_y}$ (m)	Height $\boldsymbol{w_z}$ (m)
Obstacle 1	18.0	6.5	1.0	9.0
Obstacle 2	18.0	18.0	1.0	10.0
Obstacle 3	37.5	5.5	1.0	7.0
Obstacle 4	37.5	13.0	1.0	4.0
Obstacle 5	37.5	19.0	1.0	4.0
Obstacle 6	37.5	24.5	1.0	1.0
Obstacle 7	56.0	1.5	1.0	3.0
Obstacle 8	56.0	9.0	1.0	4.0
Obstacle 9	56.0	18.0	1.0	8.0
Obstacle 10	56.0	24.5	1.0	1.0

Within this 2-D domain, automated routing was executed using the following MOGA control parameters: 50 generations, a population size of 50, a crossover ratio of 0.85, and a mutation ratio of 0.05. A single-axis floor acceleration response spectrum with a peak acceleration of 2.0 G was applied at the starting terminal. Full-scale pipe material properties corresponded to STPT410 carbon steel with outer diameter D = 318.5 mm, wall thickness t = 10.5 mm (inner diameter 297.55 mm), density ρ = 7.83 $\times$ 10^{-6} kg/mm^3, Young's modulus E = 200 GPa, and allowable stress ceiling P_{al} = 376 MPa.

The numerical synthesis results for the 1st-generation elite layout candidate and the converged 50th-generation elite candidates are schematically illustrated in Figure 7 (a) and (b).

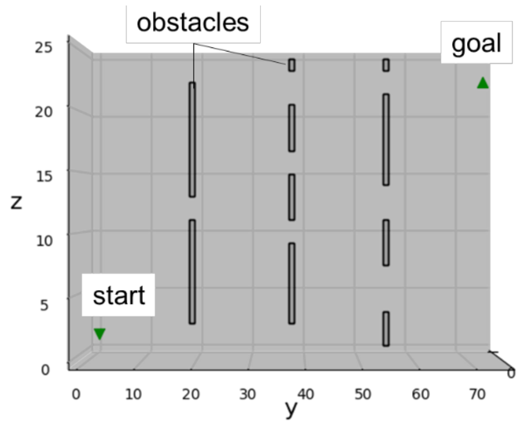

(a) Design space for 2D routing

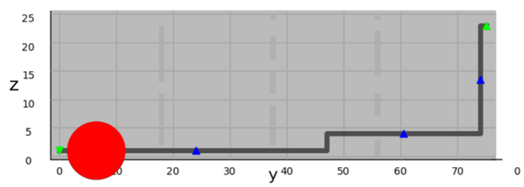

(b) Initial 1st-generation elite candidate

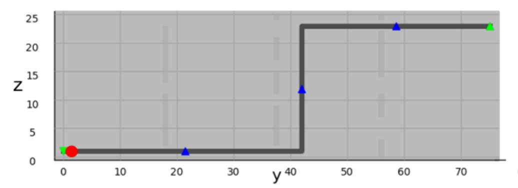

(c) Final 50th-generation elite candidate

Figure 7: 2D benchmark design domain and automated routing optimization results: (a) Design space for 2D routing, (b) initial 1st-generation elite candidate exhibiting 4 bends and excessive rigid dynamic stress (F = 87.97), and (c) final 50th-generation elite candidate featuring a 2-bends flexible detour geometry (F = 0.61).

As depicted in Figure 7(b), the 1st-generation elite layout constructed a rigid trajectory comprising 4 bends. Because this unoptimized geometry exhibited high structural stiffness, its natural frequencies coincided with the acceleration peak of the floor response spectrum, resulting in an artificially high surrogate peak dynamic bending stress metric of 21,445.29 MPa and a total evaluation index of F = 87.97.

Conversely, through 50 generations of evolutionary selection, the algorithm eliminated redundant bends and optimized support placement. As shown in Figure 7(c), the 50th-generation elite layout reduced the bend count from 4 to 2 while avoiding all 10 obstacles (P_O = 0). This geometric simplification increased topological flexibility, suppressing the surrogate peak dynamic stress metric down to 27.67 MPa and reducing the total evaluation index F to 0.61.

6.2. Similitude Scaling Laws and Shaking-Table Apparatus

To empirically evaluate the 1st- and 50th-generation layouts on a shaking table, physical-scale models were fabricated in accordance with structural similitude principles [22]. Choosing a geometric scaling factor of λ = 50, representative physical lengths l, dynamic vertical displacements Δz, and excitation time t scale as $1/\lambda$ = 1/50, natural frequencies f and input accelerations a scale as λ = 50, and system mass m scales as $1/\lambda^3$ = 1/125,000.

Under this scaling ratio $1/\lambda$ = 1/50, the full-scale prototype domain (75.0 m $\times$ 25.0 m) was transformed into a 1.5 m $\times$ 0.5 m experimental frame. Precision STPT410 carbon steel tubing with outer diameter D_{model} = 6.0 mm and wall thickness t_{model} = 0.5 mm (inner diameter 5.0 mm) was used for model fabrication. The scale model was designed for qualitative/modal similitude rather than strict stress similitude.

The experimental apparatus comprised a Brüel & Kjær 4809 electrodynamic shaker driven by a Tektronix AFG1022 function generator and a Brüel & Kjær 2706 power amplifier, delivering single-axis sinusoidal-sweep excitations (0 Hz to 45 Hz in 1 Hz increments). Non-contact optical laser displacement sensors (Keyence LB-02/LB-62, measuring range with a measuring distance of 40 mm and a linear measuring range of $\pm$10 mm) connected to a National Instruments cDAQ-9178 DAQ chassis were positioned at critical high-flexibility geometric nodes to measure localized dynamic vertical displacements Δz. Flexible tether fishing-line supports were attached to anchor points to liberate axial sliding degrees of freedom while restraining non-axial motions. The complete excitation and measurement channel layout (ch1 for input acceleration; ch2–ch4 for response nodes) and the curvature transformation geometry are schematically illustrated in Figure 8.

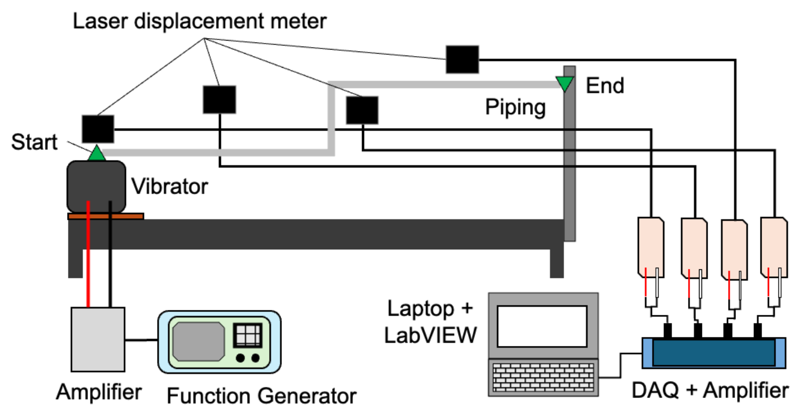

(a) **S**chematic of excitation and optical acquisition system

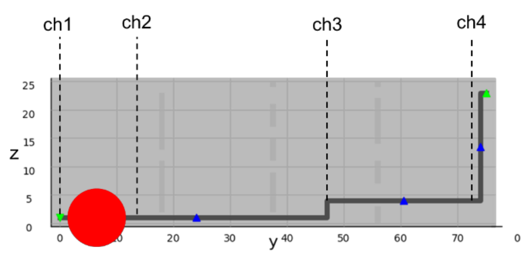

(b) 1st-generation physical model with channels ch1–ch4

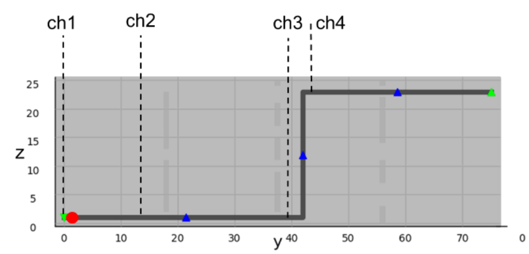

(c) 50th-generation physical model with channels ch1–ch4

Figure 8: Dynamic shaking-table experimental setup and non-contact laser measurement configuration: (a) schematic of excitation and optical acquisition system, (b) 1st-generation physical model with channels ch1–ch4, and (c) 50th-generation physical model with channels ch1–ch4.

6.3. Dynamic Frequency-Sweep Response and Assessment of Surrogate-Captured Trends

Prior to physical testing, baseline numerical modal analysis (CADTOOL Frame Structure Analysis) was performed. The 1st-generation candidate exhibited natural frequencies at f_1 = 39.62 Hz and f_2 = 42.59 Hz, whereas the 50th-generation candidate exhibited shifted fundamental modes at f_1 = 27.66 Hz and f_2 = 28.30 Hz.

The experimentally observed resonance frequencies were consistent with the modal-frequency trends predicted by the numerical model. For the 1st-generation baseline, the dominant experimental response occurred at 42 Hz, compared with the numerically predicted second natural frequency of 42.59 Hz. For the 50th-generation layout, the dominant response shifted to 26 Hz, compared with the predicted fundamental frequency of 27.66 Hz. Thus, the experiment reproduced the substantial downward modal-frequency shift predicted for the synthesized flexible-detour geometry.

For the 1st-generation baseline model, displacement amplitudes peaked at Δz = 4.04 mm (ch3) at 42 Hz, closely matching the predicted second natural frequency (f_2 = 42.59 Hz). Structural reaction feedback at resonance also caused localized input acceleration drop-offs at ch1 due to back-EMF reaction coupling with the shaker table.

Conversely, the 50th-generation layout shifted the physical resonance peak to 26 Hz (Δz = 1.99 mm at ch3 and 1.93 mm at ch4), demonstrating consistent alignment with the software-captured fundamental mode ($f_1 = 27.66$ Hz).

To convert measured vertical displacement profiles Δz into equivalent dynamic bending stresses σ_{exp}, Euler-Bernoulli beam kinematics were applied. Defining l as the distance from the sensor to the nearest support anchor, the curvature radius R of the deformed section is calculated as:

$$R \approx \frac{l^2}{8\Delta z} \tag{4}$$

Using R, D_{model}, and E, the scale-model dynamic bending stress σ_{model} is expressed by:

$$\sigma_{\mathrm{model}} = \frac{ED_{\mathrm{model}}}{2R} \tag{5}$$

Applying similitude scaling (multiplying model stress by acceleration scaling λ and length scaling $1/\lambda$), σ_{model} is converted into equivalent full-scale prototype dynamic bending stress σ_{exp} [23]. Figure 9 compares the resulting dynamic stress profiles across excitation frequencies. The quantitative comparison between surrogate predictions and experimental measurements converted to prototype scale is summarized in Table 6. As compiled in the table, physical measurements confirmed that the 50th-generation optimized layout reduced peak equivalent dynamic bending response from 22.08 MPa down to 11.98 MPa, achieving an overall physical dynamic response reduction of 45.7%.

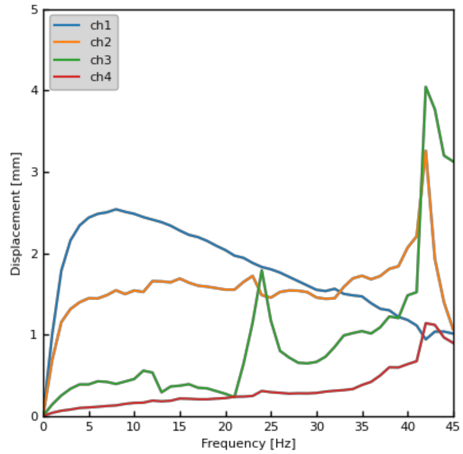

(a) 1st-generation baseline reaching peak stress at 42 Hz (ch2)

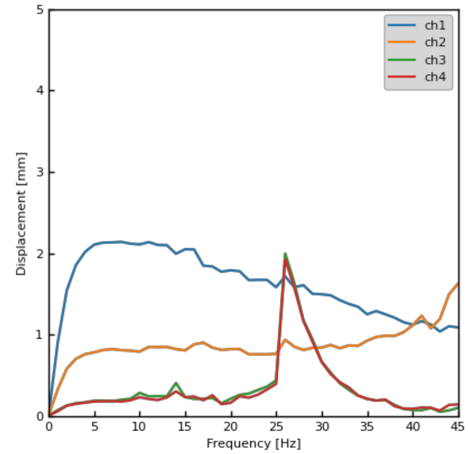

(b) 50th-generation layout demonstrating stress suppression across all channels

Figure 9: Dynamic bending stress distributions σ_{exp} across excitation frequencies (0 Hz to 45 Hz): (a) 1st-generation baseline reaching peak stress at 42 Hz (ch2), and (b) 50th-generation layout demonstrating stress suppression across all channels.

Table 6: Natural frequencies and full-scale equivalent peak dynamic stresses between response spectrum surrogate predictions and shaking-table measurements

Layout Configuration	Numerical Modal Freq. (Hz)	Experimental Peak Freq. (Hz)	Surrogate Peak Stress $S_{\max}$ (MPa)	Equivalent prototype-scale response metric (MPa)
Initial (1st Gen) Baseline	f_1 = 39.62, f_2 = 42.59	42.0	21,445.29	22.08 MPa
Optimized (50th Gen) Layout	f_1 = 27.66, f_2 = 28.30	26.0 / 45.0	27.67	11.98

Although the dynamic stress values exhibit a significant numerical discrepancy (2.14×10^4 MPa in the surrogate vs. 22.08 MPa converted from physical experiment), this divergence is physically justified by a boundary-condition mismatch. The idealized numerical surrogate assumes infinite-stiffness rigid anchors across all degrees of freedom, accumulating artificial constraint forces at resonance, whereas the physical model's flexible tether supports liberated axial sliding, thereby relieving axial force buildup during shaking. Consequently, absolute dynamic stress prediction for highly rigid topologies was not validated by the experiment.

More importantly, in the context of surrogate-assisted evolutionary computation, precise prediction of absolute fitness values is not strictly necessary. The primary mandate of a surrogate model is to serve as a robust "Ranking Tool." It must accurately preserve the ordinal superiority (the relative fitness rankings) among candidate layouts to ensure that the genetic selection operators guide the population toward the physically favorable candidate regions.

The experimental results successfully confirm this crucial capability. Despite the absolute magnitude differences induced by idealized boundary conditions, the lightweight response-spectrum surrogate successfully captured:

(1) the location of the dominant measured response;

(2) the direction and approximate magnitude of the modal-frequency shift; and

(3) the relative performance ranking between the two evaluated routing geometries.

These results support the use of the lightweight response-spectrum model as a computationally efficient screening and ranking surrogate during global routing optimization, while higher-fidelity structural analysis remains necessary for final design verification.

7. ENGINEERING WORKFLOW DEMONSTRATION AND COMPARISON WITH AN EXPERT-DESIGNED BASELINE

The dynamic and statistical evaluations executed in Part II provide critical insights into the integration of stochastic optimization and structural mechanics in plant engineering. First, the consistency of performance rankings between the simplified numerical surrogate and the physical shaking-table experiments supports the use of lightweight, linear physical indicators during the global search phase. Although the absolute stress values captured by the response-spectrum method diverge at resonance due to idealized, infinite-stiffness anchor approximations, the surrogate framework effectively indicates the relative performance trends of alternative layouts. It differentiates between rigid, resonance-vulnerable paths and flexible, seismically resilient detours. This capability is supported by scale-model testing, in which the synthesized detour geometry successfully shifted the system's natural frequencies away from excitation peaks and reduced peak dynamic bending responses. Therefore, the present experimental results should be interpreted as proof-of-concept validation of the surrogate's trend-prediction capability, rather than validation of absolute seismic stress prediction accuracy.

To evaluate the practical utility of the proposed automated synthesis framework, an engineering utility assessment benchmarked the algorithmically synthesized layout against a baseline layout manually drafted by an experienced industrial piping designer. Both the MOGA-A* framework and the human engineer were subjected to identical spatial boundary conditions, obstacle layout constraints, and equipment terminal locations specified for Case 1 (the Onagawa Nuclear Power Plant model). The comparative physical layouts are schematically illustrated in Figure 10, and the quantitative metrics are summarized in Table 7.

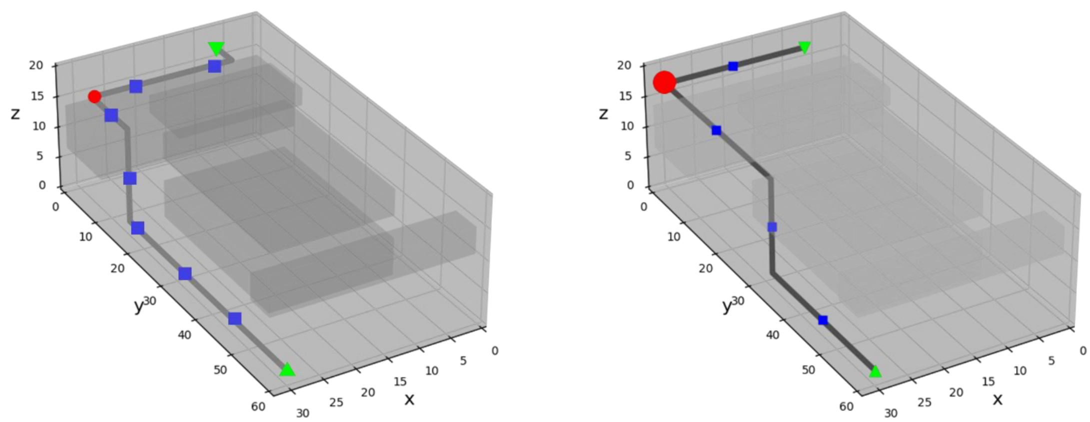

(a) Designed by experienced piping designer (b) Present study

Figure 10: Comparison of physical routing configurations: (a) layout designed by the experienced piping designer, and (b) layout synthesized by the present study.

Table 7: Quantitative Comparison Between Human (experienced engineer's baseline) and Algorithmic (MOGA-A*) Routing

Metric Parameter	Human Baseline	MOGA-A* (Present Study)
Design / Execution Mode	Manual CAD	Automated Solver (Parallel Work Possible)
Execution Time	15 minutes	46 minutes 19 seconds
Active Obstacle Collision	No	No
Peak Seismic Stress	18.63 MPa (Passed)	145.46 MPa (Passed)
Regulatory Code Compliance	Fully Compliant	Fully Compliant (Below 309 MPa allowable)

As compiled in Table 7, the peak equivalent seismic stress for the human expert's baseline was 18.63 MPa, whereas the MOGA-A* layout generated a peak dynamic stress of 145.46 MPa. While both configurations satisfied the adopted allowable seismic stress ceiling (P_{al} = 309 MPa), the experienced engineer achieved a lower dynamic stress level than the automated solver in the benchmark.

This performance discrepancy is physically explained by the density and strategic placement of structural supports. The human designer placed multiple intermediate supports along straight spans, ensuring that every sub-span remained strictly below the recommended support span threshold of l_{span} = 9.23 m. In contrast, the support placement logic implemented in the present MOGA-A* framework employs a simplified midpoint-splitting rule that places at most one support at the geometric midpoint of a straight exceeding l_{span}. This rule does not automatically insert multiple intermediate supports to ensure that all resulting sub-spans remain below the threshold.

Consequently, placing additional intermediate supports along the remaining long straight segments of the algorithmically synthesized layout would be expected to reduce the peak dynamic stress closer to the expert's baseline. Because the 3-D spatial routing path synthesized by the algorithm closely resembles the human engineer's layout, this stress difference is primarily an artifact of the simplified support placement heuristic. This indicates that while the automated framework generates code-compliant initial 3-D path geometry, refined support allocation remains an area for post-processing or algorithmic enhancement.

The practical utility of the framework lies in decision support and workflow automation. While the experienced engineer completed the single benchmark layout faster (15 minutes vs. 46 minutes), manual routing in congested 3-D environments often involves iterative spatial trials for less experienced designers. As demonstrated by the statistical evaluation in Section 5, executing parallel runs (N= 4 - 6) provides an estimated probability exceeding 95% of generating a high-performance, collision-free layout satisfying the adopted stress ceiling, while simultaneously yielding a set of alternative Pareto-optimal design drafts (e.g., layouts balancing bend count versus dynamic response). Because the framework executes autonomously, it eliminates manual spatial trial and error, enabling engineers to generate valid initial design candidates and trade-off options for detailed engineering refinement while performing parallel tasks.

8. CONCLUSIONS

This study (Part II) presented a statistical, physical, and benchmarking assessment of the hybrid MOGA-A* piping routing framework developed in Part I. Based on computational sampling, scale-model shaking-table experiments, and human expert benchmarking, the primary findings are summarized as follows:

(1) **Statistical Characterization of Search Reproducibility:** Maximum Likelihood Estimation (MLE) confirmed that structurally compliant candidate populations follow log-normal or Gamma probability distributions depending on spatial complexity. Depending on the spatial complexity regime, executing $N = 4$--6 independent parallel optimization runs for moderately congested topologies or approximately $N = 20$ runs for highly fragmented topologies yields an estimated cumulative probability exceeding 95% ($P_N \geq 95\%$) of retrieving at least one candidate layout within the predefined high-performance band.

(2) **Spatial Complexity Governance:** Global search efficiency and local-minima trapping across the examined cases were governed more strongly by the obstacle clustering index (g_{cluster}) than by total volumetric space occupancy (g_{Occ}) alone. Large, consolidated obstacle blocks preserve continuous macro-corridors that enable higher convergence rates (41.0% in Case 4), whereas fragmented obstacle networks create

narrow, disjointed corridors that increase local-minima trapping (14.0% in Case 3).

(3) **Physical Dynamic Consistency of the Surrogate Model:** Frequency-sweep shaking-table experiments on scaled models (1:50) confirmed that the lightweight response-spectrum surrogate model effectively reflects physical dynamic trends. The synthesized flexible detour layout shifted fundamental modal frequencies away from floor-resonance peaks, achieving a 45.7% reduction in peak dynamic response (11.98 MPa) compared with the unoptimized baseline (22.08 MPa). The surrogate model demonstrated consistent agreement with physical measurements regarding localized peak response nodes, modal frequency shift directions, and relative topological performance rankings.

(4) **Engineering Utility and Workflow Benchmarking:** Comparative evaluation against an experienced engineer's baseline under Onagawa Nuclear Power Plant constraints yielded a geometrically similar layout satisfying the adopted allowable seismic stress ceiling ($P_{\text{allowable}}$ = 309 MPa) in 46 minutes. Although the human expert achieved a lower peak dynamic stress (18.63 MPa vs. 145.46 MPa) by manually placing a higher density of intermediate supports, the framework autonomously generates structurally sound initial 3-D path geometry and multi-candidate Pareto design drafts, reducing manual trial and error in early-stage plant design.

In conclusion, this investigation provides a quantitative, physically consistent, and computationally efficient platform for automated decision support in early-stage piping layout synthesis. Future work may explore integrating data-driven candidate-generation strategies (e.g., geometric deep learning) to augment stochastic search operators and accelerate spatial pathfinding.

DECLARATION ON THE USE OF ARTIFICIAL INTELLIGENCE (AI) TOOLS

The authors utilized the Gemini large language model (Google LLC) and Grammarly (Grammarly, Inc.), accessed via a web browser environment in June 2026, exclusively for language editing, structural refinement, and text readability improvements. No substantive research content, data, or conclusions were generated by these tools. The authors verified all outputs and assumed full responsibility for the paper's technical integrity.

ACKNOWLEDGMENT

The authors deeply express their gratitude to Professor Emeritus Shigehiko Kaneko (The University of Tokyo), Dr. Yuichi Yoshida (National Research Institute of Fire and Disaster), and Mr. Susumu Yamaguchi (Kawasaki Heavy Industries, Ltd.) for their invaluable technical discussions, insightful comments, and constructive feedback throughout the course of this structural and algorithmic investigation.

A preliminary version of this research was presented at the ASME 2024 International Mechanical Engineering Congress and Exposition (IMECE2024-144011). This manuscript, together with Part I, represents the full-length journal version of that work.

AUTHOR CONTRIBUTIONS

Shunta Mogi: Software (Algorithm programming), Investigation (Conducting physical experiments and numerical simulations), Formal Analysis, Writing - Original Draft. Akane Uemichi: Conceptualization, Methodology, Supervision, Project Administration, Writing - Original Draft, Writing - Review & Editing. Naoya Takamura: Validation, Visualization.

FUNDING

No funding was received for this research.

CONFLICT OF INTEREST

The authors declare that they have no known competing financial interests or personal relationships that could have appeared to influence the work reported in this paper.

DATA AVAILABILITY STATEMENT

The primary data supporting the engineering findings of this study are available within the article. The raw datasets generated and analyzed during the evolutionary optimization process are available from the corresponding author upon reasonable request.

NOMENCLATURE

a	Input acceleration, m/s^2
D	Outer diameter of prototype piping section, mm
D_{model}	Outer diameter of the piping scale model, mm
E	Young's modulus of the piping material, GPa
F	Overarching total evaluation index / objective function
f	Dynamic natural frequency, Hz
g_{DSR}	Designable space ratio
g_{Occ}	Space occupancy index
$g_{cluster}$	Obstruction clustering index
l	Cumulative physical length of the synthesized piping layout, m, or distance from sensor to nearest support anchor, mm
L_y, L_z	Global dimensional boundaries of the rectangular experimental search space, m
$n_{cluster}$	Number of distinct obstacle groups / clusters
P	Single-Run High-Performance Success Probability
P_{95}	Statistical confidence level of synthesizing at least one high-performance candidate layout ($\geq$ 95%)
P_O	Penalty function of obstacle interference
P_{al}	Code-defined design allowable seismic stress threshold, Pa
R	Curvature radius of the piping bend, mm
R^2	Coefficient of determination for Maximum Likelihood Estimation (MLE) fit

S_{max} Peak equivalent stress of the piping layout, Pa

t_{model} Nominal wall thickness of the scale pipe section, mm

V Total design space volume, m^3

V_{obs} Total volume of obstacles, m^3

w_x, w_y, w_z Bounding dimensions (width, length, height) of solid obstacles, m

x, y, z Spatial Cartesian coordinates, m

x_s, y_s, z_s Starting terminal nozzle coordinates, m

x_e, y_e, z_e Ending terminal nozzle coordinates, m

Greek Characters

Δz Physical dynamic displacement measured by the laser sensor, mm

λ Geometric scaling factor for structural similitude

μ_V Mean volume ratio of obstacles to total design space

σ_{exp} Full-scale prototype equivalent dynamic bending stress converted from physical measurements, MPa

σ_{model} Dynamic bending stress of physical scale model, MPa

σ_V Variance parameter of obstacle volume distribution

REFERENCES

[1] Blokland, M., et al., 2023, "Literature Survey on Automatic Pipe Routing," *Operations Research Forum*, 4(1), p. 35. https://doi.org/10.1007/s43069-023-00208-5

[2] Zhou W & Nessim MA, 2011, Optimal Design of Onshore Natural Gas Pipelines, *J. Pressure Vessel Technol*., 133(3): 031702 https://doi.org/10.1115/1.4002496

[3] Zhao B et al. Optimization of Protection Device Parameters for Pump-Stopping Water Hammer Protection in Long-Distance Water Conveyance Pipelines Via Hybrid NSGA-II, *J. Pressure Vessel Technol.* Jun 2026, 148(3): 031401 https://doi.org/10.1115/1.4070901

[4] Ito, T., 1999, "A Genetic Algorithm Approach to Piping Route Path Planning," *J. Intell. Manuf.*, 10(1), pp. 103–114. https://doi.org/10.1023/A:1008924832167

[5] Sandurkar, S., and Chen, W., 1999, "GAPRUS—Genetic Algorithms Based Pipe Routing Using Tessellated Objects," *Comput. Ind.*, 38(3), pp. 209–223. https://doi.org/10.1016/S0166-3615(98)00130-4

[6] Dong, Z., and Bian, X., 2020, "Ship Pipe Route Design Using Improved A* Algorithm and Genetic Algorithm," *IEEE Access*, 8, pp. 153273–153296. https://doi.org/10.1109/ACCESS.2020.3018288

[7] Shirakawa, M., and Arakawa, M., 2018, "Multi-Objective Optimization System for Plant Layout Design (3rd Report, Interactive Multi-Objective Optimization Technique for Pipe Routing Design)," *J. Adv. Mech. Des. Syst. Manuf.*, 12(2), p. JAMDSM0053. https://doi.org/10.1299/jamdsm.2018jamdsm0053

[8] Wei Z., et al., 2024, "The Intelligent Layout of the Ship Piping System Based on A*-Genetic Algorithm," *Appl. Sci.,* 14(7), 2694. https://doi.org/10.3390/app14072694

[9] Mogi, S., and Uemichi, A., "Automated 3D Piping Routing Synthesis Considering Seismic Resilience: Part I—Mathematical Formulation and Layout Optimization Framework," EngineerXiv Preprint, https://doi.org/10.31224/8125

[10] Japan Electric Association, 2017, Technical Code for Seismic Design of Nuclear Power Plants, JEAC 4601-2015.

[11] ASME, 2023, ASME Boiler and Pressure Vessel Code, Section III: Rules for Construction of Nuclear Facility Components, American Society of Mechanical Engineers, New York.

[12] Abe H & Chokshi N, Overview of Nuclear Piping Seismic Verification, *J. Pressure Vessel Technol.* Jun 2022, 144(3): 031903 https://doi.org/10.1115/1.4053831

[13] Ryu YH, et al. 2019, Fragility Evaluation in Building-Piping Systems: Effect of Piping Interaction With Buildings, *J Pressure Vessel Technol*. 141(1): 010906 https://doi.org/10.1115/1.4039004

[14] Mogi, S., and Uemichi, A., 2024, "Automatic Piping Routing Applying Multi-Objective Genetic Algorithm," *Proc. ASME 2024 Int. Mech. Eng. Congr. Expo. (IMECE2024),* Portland, OR, USA, Paper No. IMECE2024-144011. https://doi.org/10.1115/IMECE2024-144011

[15] Deb, K., Pratap, A., Agarwal, S., and Meyarivan, T., 2002, "A Fast and Elitist Multiobjective Genetic Algorithm: NSGA-II," *IEEE Trans. Evol. Comput.*, 6(2), pp. 182–197. https://doi.org/10.1109/4235.996017

[16] Jin, Y., 2011, "Surrogate-Assisted Evolutionary Computation: Recent Advances and Future Challenges," *Swarm Evol. Comput.,* 1(2), pp. 61–70. https://doi.org/10.1016/j.swevo.2011.05.001

[17] Malan, K. M., and Engelbrecht, A. P., 2013, "A Survey of Techniques for Characterising Fitness Landscapes," *Inf. Sci.*, 229, pp. 56–64. https://doi.org/10.1016/j.ins.2013.04.015

[18] Hansen, N., et al., 2010, "Real-Parameter Black-Box Optimization Benchmarking: Experimental Setup," *Proc. 12th Annu. Conf. Comp. Genet. Evol. Comput. (GECCO '10)*, pp. 1689–1696.

[19] Suzuki K et al., 2002, Seismic Proving Test of Ultimate Piping Strength: Test Results on Piping Component and Simplified Piping System, *ASME 2002 Pressure Vessels and Piping Conference*, PVP2002-1403, pp. 99-106. https://doi.org/10.1115/PVP2002-1403

[20] Lee JB et al., Pipe Routing of Offshore Structure Considering Space Availability, *Korean J Comp Design Eng*, 24.3, 2019, pp.280-288. https://doi.org/10.7315/CDE.2019.280

[21] Datta, T. K., 2010, Seismic Analysis of Structures, John Wiley & Sons, Singapore.

[22] Wakita E & Wakita T, Estimate Method of Damping Characteristic And Applicability Between Different Size Structures, *J Struc Construction Eng (Trans AIJ)*, 2009, 74 (644), 1731-1739 https://doi.org/10.3130/aijs.74.1731 (in Japanese)

[23] Tsuji T et al. Development of the method to measure vibrational stress of small-bore piping with contactless displacement sensor: accuracy confirmation by vibrational experiment using branch pipe, *INSS Journal* (20) 2013, 95-108 (in Japanese)

Figure Caption List

Figure 1: Distribution of the normalized space occupancy index $gOcc$ against the total volume ratio of obstacles, modeled as a log-normal distribution peaking at $\mu V = 0.5$.

Figure 2: 3-D distribution of the Designable Space Ratio $gDSR$ plotted against the space occupancy ratio $gOcc$ and the number of obstacle clusters $gcluster$.

Figure 3: 3D spatial layout of obstacles and synthesized routing corridors.

Figure 4: Probability density distributions of overarching evaluation index F and final generational elite solutions showing unimodal and bimodal convergence patterns.

Figure 5: Histogram and cumulative ratio of total evaluation index F for Case 2 under an elevated mutation probability of 10%.

Figure 6: Histogram and cumulative ratio of total evaluation for Case 4

Figure 7: 2D benchmark design domain and automated routing optimization results: (a) Design space for 2D routing, (b) initial 1st-generation elite candidate exhibiting 4 bends and excessive rigid dynamic stress (F = 87.97), and (c) final 50th-generation elite candidate featuring a 2-bend flexible detour geometry (F = 0.61).

Figure 8: Dynamic shaking-table experimental setup and non-contact laser measurement configuration: (a) schematic of excitation and optical acquisition system, (b) 1st-generation physical model with channels ch1–ch4, and (c) 50th-generation physical model with channels ch1–ch4.

Figure 9: Dynamic bending stress distributions σexp across excitation frequencies (0 Hz to 45 Hz): (a) 1st-generation baseline reaching peak stress at 42 Hz (ch2), and (b) 50th-generation layout demonstrating stress suppression across all channels.

Figure 10: Comparison of physical routing configurations: (a) layout designed by the experienced piping designer, and (b) layout synthesized by the present study.

Table Caption List